Research Square

Preprints are preliminary reports that have not undergone peer review.
They should not be considered conclusive, used to inform clinical practice,
or referenced by the media as validated information.

Coordinated Optimization of Grid-Forming Control in LCC-MMC Hybrid DC Transmission Systems Considering Virtual Power Angle Evolution Mechanism

Weiming Zhang

858436030@qq.com

State Grid Hebei Electric Power Research Institute

Qingquan Liu

State Grid Hebei Electric Power Research Institute

Yongliang Chang

State Grid Hebei Electric Power Research Institute

Shaofei Guo

State Grid Hebei Electric Power Research Institute

Ze Li

State Grid Hebei Electric Power Research Institute

Research Article

Keywords: hybrid direct current transmission, grid-forming control, grid-following control, virtual power angle, power regulation, smooth switching

Posted Date: August 3rd, 2026

DOI: https://doi.org/10.21203/rs.3.rs-10505234/v1

License: This work is licensed under a Creative Commons Attribution 4.0 International License.
Read Full License

Additional Declarations: No competing interests reported.

Coordinated Optimization of Grid-Forming Control in LCC-MMC Hybrid DC Transmission Systems Considering Virtual Power Angle Evolution Mechanism

Weiming Zhang, Qingquan Liu, Yongliang Chang, Shaofei Guo, and Ze Li are with the State Grid Hebei Electric Power Research Institute, Shijiazhuang 050021, China.

***Abstract* — To address the transient instability issue of grid-forming (GFM) control in LCC-MMC ultra-high-voltage hybrid DC transmission systems with hierarchical connection at the receiving end—where current limiting tends to lock the converter into current-source mode during AC faults—this paper proposes a coordinated optimization control strategy based on the virtual power angle. The virtual power angle characteristic equation of the GFM converter is first established, and the evolution mechanism of the virtual power angle before and after current saturation is analyzed. Based on the equal-area criterion, the analytical relationship between the critical clearing angle and the active power setpoint is derived. On this basis, a dynamic power reduction control strategy based on surplus power is proposed, which detects the unbalanced power of the converter station during faults and adaptively adjusts the power setpoint of the P-f control, thereby actively increasing the critical clearing angle. Meanwhile, for scenarios where the virtual power angle exceeds the critical value, a feedforward compensation-based smooth switching control strategy between grid-following (GFL) and GFM modes is designed to ensure the continuity of the inner-loop current reference at the switching instant. PSCAD/EMTDC simulation results demonstrate that the proposed dynamic power reduction strategy exhibits smaller transient disturbances and shorter recovery time compared with the fixed power reduction scheme, while the smooth switching strategy effectively prevents the converter from being locked into current-source mode, significantly enhancing the system's transient stability under severe faults.**

***Index Terms* — hybrid direct current transmission, grid-forming control, grid-following control, virtual power angle, power regulation, smooth switching.**

I. Introduction

In recent years, the share of renewable energy generation has continued to increase, placing higher demands on the stability and flexibility of long-distance, high-capacity transmission systems [1].Ultra-high-voltage direct current (UHVDC) transmission technology, characterized by high efficiency and flexible power regulation, has become a core technology for renewable energy delivery and cross-regional grid interconnection. Among these, the hybrid DC transmission system with hierarchical connection at the receiving end—employing a line-commutated converter (LCC) at the sending end and a modular multilevel converter (MMC) at the receiving end—combines the cost-effectiveness of LCC with the flexibility of MMC, and has demonstrated broad application prospects in numerous projects [2–3].However, the receiving-end grid often exhibits a strong-DC/weak-AC characteristic [4], posing new challenges to the safe and stable operation of the system.

Currently, the control modes of MMCs at the receiving end of hybrid DC transmission systems are mainly classified as GFL control and GFM control. GFL control relies on a phase-locked loop (PLL) for synchronization and offers proven low-voltage ride-through (LVRT) capability during faults. However, in weak grids with reduced system inertia and non-negligible grid impedance, it faces the risk of degraded synchronization stability or even loss-of-lock [5].GFM control draws on the operating principles of synchronous generators: by emulating the rotor motion equations, it directly controls the amplitude and phase of the converter output voltage to actively support system voltage and frequency, thereby improving operational stability in weak grids [6–8].Reference [9] systematically compares GFM and GFL controls in terms of event response, synchronization strategy, and applicable scenarios. Reference [10] systematically reviews the stability of GFM converters across three aspects: steady-state operating point existence, small-signal stability, and large-signal stability.

However, GFM control faces particular transient instability risks under fault conditions. Reference [11] reveals the intrinsic connection between the transient

synchronization stability of grid-connected converters and the power-angle stability of synchronous generators in terms of research methodology, and summarizes the major forms of transient instability in GFM control under large disturbances. Reference [12] points out that VSG-based GFM control incorporates multiple limiters, making it a complex switching system. Upon triggering of the current limiter, the external characteristics of the GFM converter switch from a voltage source to a current source, weakening its transient voltage support capability and exposing the system to the risk of transient synchronization instability.

To address this challenge, previous studies have focused on the virtual power angle characteristics. Reference [13] defined the virtual power angle, analyzed its characteristics before and after current saturation, and revealed the instability mechanism during the transition from voltage-source mode to current-source mode. Reference [14] derived the analytical expression of the critical clearing angle (CCA) based on the piecewise equal-area criterion, providing a theoretical basis for enhancing the transient stability of GFM control using the virtual power angle. Existing research has laid the foundation for transient stability analysis of GFM control. However, most studies focus on qualitative analysis of virtual power angle characteristics, with insufficient discussion on how to utilize the critical criterion to optimize control strategies and a lack of solutions to prevent system instability under severe faults.

To this end, this paper takes a ±800 kV bipolar LCC-MMC hybrid hierarchically-connected DC transmission system as the research object and proposes a coordinated optimization control strategy based on the CCA. First, the virtual power angle characteristic equation of the GFM converter is established, the evolution mechanism of the virtual power angle before and after current saturation is analyzed, and the CCA calculation formula is derived. On this basis, this paper proposes a dynamic power reduction control strategy based on surplus power, which detects the unbalanced power at the converter station during faults and adaptively adjusts the power setpoint of the P-F control loop in real time to increase the CCA. Meanwhile, for cases where the virtual power angle exceeds the critical value during severe faults, a feedforward compensation-based smooth switching control from GFM to GFL is implemented to prevent the converter from being locked into current-source mode. Finally, a system model is built on the PSCAD/EMTDC platform, and the effectiveness of the proposed strategy is validated through multiple fault scenarios.

II. Topology and Control Strategy of Hybrid HVDC Transmission System

A. System Topology

As shown in Fig. 1, the sending-end positive-pole and negative-pole converter stations of this bipolar hybrid HVDC system each consist of two series-connected 12-pulse LCCs. At the receiving end, each pole of the MMC station comprises two series-connected MMCs, i.e., a high-end and a low-end unit, which are connected to AC grids of different voltage levels, forming a hierarchically-connected structure. The system has a DC voltage of ±800 kV, a DC current of 2.5 kA, and a rated transmission power of 4,000 MW.

The sending-end LCC station adopts constant DC voltage control to establish and maintain the DC voltage reference of the system [15].Among the four MMC converters at the receiving end, converters I and III adopt GFM control based on virtual synchronous generators (VSG), while converters II and IV adopt constant active power control. The proposed hybrid control scheme has the following advantages: Converters I and III are connected to the high-end and low-end AC grids, respectively, providing active inertia and voltage support to two AC systems of different voltage levels simultaneously, thus effectively suppressing frequency and voltage fluctuations; Meanwhile, GFM converters are deployed in both the positive- and negative-pole series-connected converters. Their voltage-source external characteristics help maintain DC-port voltage stability and provide a stable voltage reference for the constant-power converters of the same pole, thereby improving voltage balancing among valve groups and enhancing

the overall stability of the DC system [16]

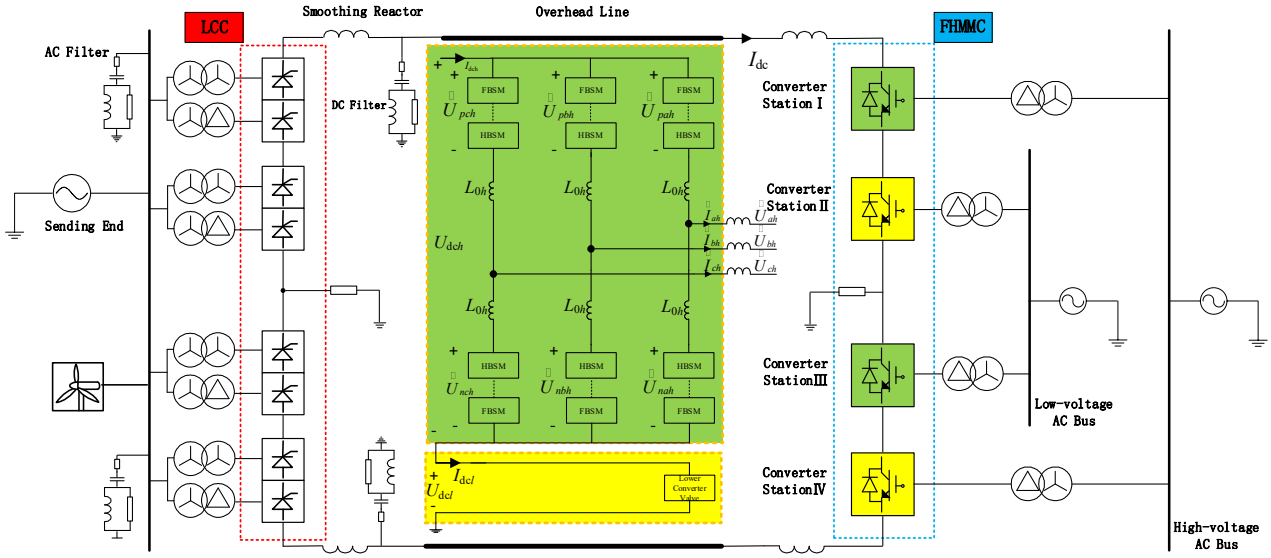


Fig. 1. Topology of the hybrid HVDC transmission system

B. Control Strategy of Grid-Forming Converter

The sampling, voltage/current control, and PWM signal generation of a GFM converter are identical to those of a conventional GFL converter; the difference lies in the power outer-loop control. GFM control emulates the electromechanical transient characteristics of a synchronous generator to directly control the amplitude and phase of the output voltage, thereby autonomously establishing the AC voltage and providing inertia and damping support to the system [17].Its power outer loop mainly consists of two components: P-f control and Q-V control, which generate the phase and amplitude of the internal electromotive force (emf), respectively.

The P-f control emulates the rotor motion equation (i.e. the swing equation) of a synchronous generator. It detects the deviation between the output active power and the setpoint to generate the angular frequency of the VSG, which is then integrated to obtain the phase reference of the output voltage. The rotor motion equation is given as follows:

$$J\frac{d\Delta\omega}{dt}+D\Delta\omega=\left(P_{\mathrm{ref}}-P_{\mathrm{e}}\right)/\omega_0 \qquad (1)$$

where J is the virtual inertia coefficient, D is the damping coefficient, $\omega$is the output angular frequency of the VSG, and $\omega_0$is the rated angular frequency of the grid. P_{ref} denotes the active power setpoint, and P_{e} denotes the actual output active power.

Due to differences in control parameters and measurement errors, DC voltage imbalance exists between the high-end and low-end converters. To address this, a voltage balancing control loop is introduced into the P-f control loop of the GFM control. The DC voltage deviation $\Delta U_{\mathrm{dc,pu}}$ between the high-end and low-end converters is detected, and together with the per-unit DC current $I_{\mathrm{dc,pu}}$, the power imbalance $\Delta P_{\mathrm{dc,pu}}$ is calculated, as given in Eq. (2) [18].

$$\Delta P_{\mathrm{dc,pu}}=\Delta U_{\mathrm{dc,\ pu}}I_{\mathrm{dc,pu}}P_{\mathrm{ref0,pu}} \qquad (2)$$

This correction is superimposed on the active power setpoint, yielding the updated power reference $P_{\mathrm{ref,pu}}$, as given in Eq. (3).

$$P_{\mathrm{ref,pu}}=\Delta P_{\mathrm{dc,pu}}+P_{\mathrm{ref0,pu}} \qquad (3)$$

Substituting the updated power reference into Eq. (1) enables dynamic adjustment of the GFM converter's power output, thereby suppressing voltage deviations between valve groups. The P-f control loop incorporating the voltage-balancing link is shown in Fig. 2.

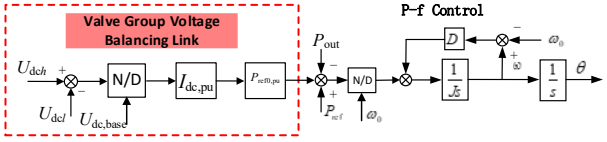


Fig. 2. Block diagram of active power-frequency control

The Q-V control emulates the excitation regulation characteristics of a synchronous generator to generate the internal voltage amplitude E based on the reactive power deviation and terminal voltage deviation. The control equation is given by:

$$K_{\mathrm{q}}(Q_{\mathrm{ref}}-Q_{\mathrm{out}})+K_{\mathrm{V}}(V_{\mathrm{ref}}-V_{\mathrm{f}})=0 \tag{4}$$

where Q_{ref}、Q_{out} are the reactive power setpoint and actual value, respectively; V_{ref}、V_{f} are the AC voltage reference and actual value, respectively; K_{q} is the reactive power droop coefficient, with K_{q}=0 corresponding to constant voltage control; K_{V} is the voltage droop coefficient, with K_{V}=0 corresponding to constant reactive power control [19]. When both K_{q} and K_{V} are nonzero, it becomes reactive power – voltage droop control. The Q-V control loop is shown in Fig. 3.

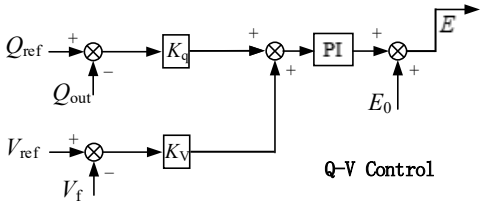


Fig. 3. Block diagram of reactive power-voltage control

The internal voltage reference $E\angle\theta_0$ generated by the P-f control and Q-V control loops is converted into inner-loop current references via virtual admittance control, enabling fast tracking of the current control loop. Virtual admittance control reshapes the port impedance characteristics of the converter by adjusting the virtual resistance Rv and virtual inductance Lv, thereby improving its interactive stability with the AC grid and maintaining a good phase margin under varying grid strengths [20].

In summary, the block diagram of the VSG-based GFM control proposed in this paper is shown in Fig. 4, which mainly includes P-f control, Q-V control, virtual admittance control, and dual-loop current control [13].In Fig. 4, u_{sd}、u_{sq} are the d- and q-axis components of the grid voltage, respectively; i_{sd}、i_{sq} are the d- and q-axis components of the converter output current, respectively; and L_{f} is the equivalent inductance of the converter.

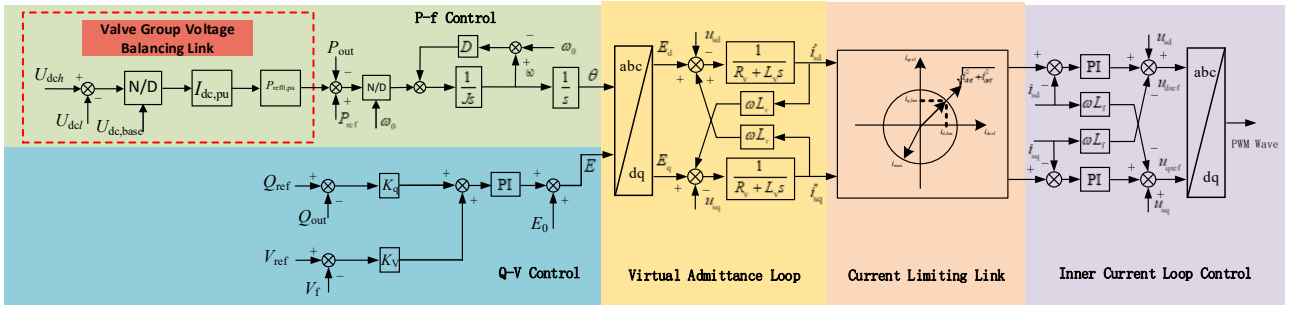


Fig. 4. Block diagram of VSG-based grid-forming control

III. Transient Stability Analysis of Grid-Forming Control

A. *Definition and Characteristic Equation of Virtual Power Angle*

The power angle δ of an inverter is the angle between its output voltage $\dot{V}$ and the grid voltage $\dot{U}$, while the virtual power angle δ' is defined as the angle between the d-axis and the grid voltage. Under steady-state conditions, the converter output voltage is aligned with the d-axis; thus, the actual power angle equals the virtual power angle. The vector relationship is illustrated in Fig. 5.

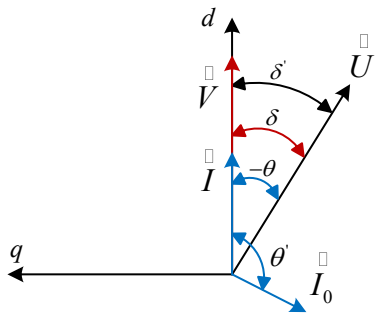


Fig. 5. Vector diagram of related variables

In Fig. 5, $\dot{I}_0$ is the current of the equivalent current source of the grid, the grid-side power factor angle θ is the angle between the grid voltage and the converter output current, and θ' is the power angle under current saturation of the converter. Let α be the angle between the d-axis and $\dot{V}$, and β the angle between the d-axis and the converter output current $\dot{I}$.The following relationships can be obtained from Fig. 6:

$$\alpha = \arctan(\frac{-V_q}{V_d}) = \delta' - \delta \tag{5}$$

$$\beta = \arctan(\frac{I_q}{I_d}) = -\theta - \delta' \tag{6}$$

where V_d and V_q are the d- and q-axis components of $\dot{V}$, respectively, and U_d and U_q are the d- and q-axis components of $\dot{U}$. The virtual power angle characteristic equation of the converter is given by Eq. (7):

$$P_E = \frac{|\dot{U}||\dot{V}|}{X_\Sigma}\sin\delta = P_{um}\sin(\delta' - \alpha) \tag{7}$$

where X_Σ is the line reactance, and P_{um} is the amplitude of the unsaturated virtual power angle curve.

Under steady-state conditions, V_d=0. From Eq. (5), it can be obtained that α=0, and thus Eq. (7) simplifies to:

$$P_{out} = P_{um}\sin\delta' \tag{8}$$

Thus, the virtual power angle characteristic curve under unsaturated current conditions is obtained, as shown in Fig. 6, where A is the stable equilibrium point.

When the inner-loop current reference reaches the limiting value, the converter can be considered as a controlled current source, and its virtual power angle characteristic transforms to:

$$P_{out} = \frac{|\dot{I}||\dot{I}_0|}{B_\Sigma}\sin\theta' = P'_{sm}\sin(\delta' + \beta + 90^\circ) \tag{9}$$

where P'_{sm} is the amplitude of Saturated Virtual Power Angle Curve 3, $\dot{I}_0 = -\mathrm{j}\dot{U}X_\Sigma^{-1}$; $B_\Sigma = X_\Sigma^{-1}$.

Once current saturation is reached, the d-axis current gradually increases to i_{max}, while the q-axis current decreases to zero. At this point, β=0 and I=i_{max}; therefore, Eq. (9) can be simplified as:

$$P_{out} = I_{max}|\dot{U}|\sin(\delta' + 90^\circ) = P'_{sm}\sin(\delta' + 90^\circ) \tag{10}$$

From Eq. (10), the virtual power angle characteristic curve of the converter under saturated conditions is obtained, as shown in Fig. 6, where D is the unstable equilibrium point.

B. Transient Operating Characteristics of Virtual Power Angle

As described in Section 2.1, when a fault occurs on the receiving-end AC bus, the inner-loop current reference increases. If the current limiting link is triggered, the converter enters the current saturation state and is equivalent to a current source. The operating point jumps from the stable equilibrium point A on Curve 1 to point A′ on fault Curve 3.At this point, since the amplitude P_{sm} of saturated virtual power angle Curve 3 is less than P_{ref}, the virtual power angle increases along Curve 3 [21], as shown in Fig. 6.

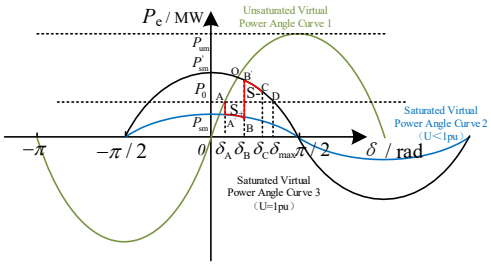


Fig. 6. Virtual power angle curves of the converter

When the virtual power angle increases to point B, the fault is cleared, the grid voltage recovers to 1.0 p.u., and the operating point switches from point B on Curve 3 to point B′ on Curve 2.Affected by virtual inertia, the power angle continues to increase until the acceleration area S_+ equals the deceleration area S_-.According to the equal-area criterion, the power angle begins to decrease along Curve 2 from point C to point O. Then the current withdraws from saturation, and the system gradually returns to point A along Curve 1, restoring stability.

As shown in Fig. 6, if the virtual power angle exceeds δ_{max} along Curve 2, then P_{out}<P_{ref}, and a new deceleration region is formed. There exists a critical angle δ_{cca} such that, when the fault is cleared at this angle, the acceleration area S_+ exactly equals the deceleration area S_- enclosed from δ_{cca} to point D.δ_{cca} is

denoted as the CCA, and the corresponding fault duration is the CCT.

According to the equal-area criterion, the acceleration area bounded by the saturated virtual power angle Curve 3 from the stable equilibrium point A to the critical clearing angle and the rated power should equal the deceleration area bounded by the saturated virtual power angle Curve 2 from the critical clearing angle to the operating point D. The expression is given in Eq. (11).

$$\int_{\delta_A}^{\delta_{cca}} \left(P_0 - \left|\dot{I}\right|\left|\dot{U}\right|\cos\delta \right) \mathrm{d}\delta = \int_{\delta_{cca}}^{\delta_D} \left(\left|\dot{I}\right|\cos\delta - P_0 \right) \mathrm{d}\delta \quad (11)$$

By integrating both sides of Eq. (11), CCA expression is obtained as

$$\delta_{cca} = \arcsin\left(\frac{P_0\delta_A - P_0\delta_D + \left|\dot{I}\right|\sin\delta_D - \left|\dot{I}\right|\left|\dot{U}\right|\sin\delta_A}{\left|\dot{I}\right| - \left|\dot{I}\right|\left|\dot{U}\right|}\right) \quad (12)$$

The analysis shows that when $\delta_B<\delta_{cca}$, there exists $\delta_C<\delta_{max}$ such that $S_+= S_-$, and the converter restores stable operation after a transient process. When $\delta_B>\delta_{cca}$, as the virtual power angle reaches point D with $S_+ > S_-$, the converter will undergo transient instability.

The above analysis applies to the case where the outer-loop power setpoint satisfies $P_{sm} <P_{ref}<P'_{sm}$.If the virtual power angle at the instant of fault clearing is less than the CCA, the system can restore stability. However, as shown in Eq. (12), a grid voltage dip reduces the amplitude of the saturation curve. Consequently, two additional cases exist: $P_{ref}<P_{sm}$ and $P_{ref}>P'_{sm}$.

When $P_{ref}<P_{sm}$, the limiting link does not activate, the current remains unsaturated, and the system continues to operate along Unsaturated Curve 1, along which it restores stability directly after fault clearing.

When $P_{ref}>P'_{sm}$, the limiting link is activated, and the operating point switches from Curve 1 to Curve 3, along which it continues to move downward. After fault clearing, the voltage recovers and the operating point transfers to Curve 2. However, due to the lack of a deceleration mechanism, the system continues to move along Curve 2, eventually resulting in transient instability.

Furthermore, if the system operating point lies in the region on Unsaturated Curve 1 beyond point O in Fig. 6, where the output current would exceed i_{max}, no limiting action actually occurs. The maximum active power output of the converter is thus given by:

$$P_{max} = \frac{P_{um}P'_{sm}}{\sqrt{P_{um}^2 + P'^2_{sm}}} \quad (13)$$

As shown in Fig. 6, P_{max} at point O is slightly less than P'_{sm} .It can be approximated that $P_{max}\approx P'_{sm}$. Therefore, considering the limiting effect, the stability margin range of the P-f control power setpoint is [0，P'_{sm}].

The sending-end converter adopts constant DC voltage control to maintain the rated DC voltage. When a fault occurs on the receiving-end AC bus, the faulty converter generates DC overvoltage due to power surplus. Since the total DC voltage across the high-end and low-end converters remains constant, the voltage of the non-faulty converters decreases. Under the effect of voltage-balancing control, the active power setpoint of the faulty converter is forced to increase, making the system more susceptible to being locked in current-source mode and ultimately leading to transient instability.

IV. Transient Stability Optimization Strategy for Grid-Forming Control

A. Transient Instability Mechanism and Optimization Approach

As discussed in Section 2.2, when current limiting is not activated, the external characteristic of the GFM converter can be regarded as voltage-source mode, with the operating point consistently following Curve 1 and eventually returning to the stable equilibrium point. However, when current limiting is activated, the external characteristic of the GFM converter switches to current-source mode. If the virtual power angle increases to the CCA and the fault persists, the system will operate along Curve 3, with the GFM converter locked in current-source mode. This will lead to transient instability, and the system remains difficult to restore even after the fault is cleared.

The CCA characterizes the system′s ability to withstand fault disturbances: the larger the CCA, the wider the allowable swing range of the virtual power angle, and the longer the CCT. Therefore, under the same fault disturbance, increasing the CCA enables the system to restore stability even if the fault is cleared slightly later, thereby preventing the GFM converter from being locked in current-source mode. As shown in Eq. (13), the CCA is inversely proportional to the

rated power of the system. The larger the rated power, the smaller the CCA, and the system may become unstable even under short-duration faults. However, since the AC voltage during the fault is determined by the fault severity and the system has already activated the current limiting, the current remains at the limit value. Therefore, actively reducing the power setpoint of the P-f control during the fault period can effectively increase the CCA and extend the CCT.

However, if a fault is not cleared in a timely manner or a severe fault occurs, the virtual power angle may still exceed the critical value, even if the power setpoint has been reduced to its lower limit, potentially leading to transient instability. When the converter operates in GFL mode, active and reactive power can be independently controlled, with active power determined by the d-axis current and reactive power by the q-axis current. Meanwhile, the PLL tracks the grid voltage phase, thereby avoiding the instability risk associated with autonomous phase regulation of the GFM control. After fault clearing, the current limiting is deactivated. Active and reactive power are rapidly readjusted via outer-loop control according to preset power references, which in turn regulate the inner-loop current to eliminate power deviations and restore power. Moreover, this process effectively suppresses current surges and power oscillations during restoration. Therefore, during a fault, the converter can be switched from GFM to GFL control, leveraging the more mature LVRT capability of GFL control to accelerate system restoration.

B. Dynamic Power Reduction Control Based on Surplus Power

As discussed above, reducing the power setpoint during a fault can effectively increase the CCA and enhance the transient stability of GFM converters. However, if the reduction is too small, it cannot provide sufficient stability margin; if too large, it may further reduce the converter output power, aggravate the power imbalance between the sending and receiving ends, and even delay post-fault voltage recovery. Therefore, the power setpoint should be dynamically adjusted based on the fault severity.

After the rated power setpoint is reduced during a fault, the acceleration area bounded by the saturated virtual power angle Curve 3 from the stable equilibrium point A to the original CCA and the reduced power setpoint decreases significantly, while the deceleration area remains unchanged, with the deceleration area now exceeding the acceleration area. The reduction in the acceleration area also leaves room for increasing the CCA, ensuring that the converter can avoid transient instability caused by the virtual power angle exceeding the limit value when subjected to faults of the same severity, even if fault clearing is slightly delayed.

When a fault occurs on the receiving-end AC bus, the AC voltage drops rapidly, and the power output of the receiving-end converter is limited. However, due to the response delay of the sending-end converter, it continues to deliver power to the receiving-end side, causing surplus power and DC overvoltage at the receiving-end converter station. The more severe the AC-side fault, the greater the surplus power and the higher the DC overvoltage. Therefore, the surplus power of the converter station can characterize the severity of the AC fault, based on which the power setpoint can be dynamically adjusted.

When a fault occurs on the receiving-end AC bus at t=0, the converter submodules begin to charge. Assuming that all submodule capacitor voltages in each arm are identical and neglecting the equivalent arm resistance R_{eq}, the voltage variation of the arm submodules can be expressed as [22]:

$$\begin{aligned}\Delta W_{MMC} &= \int_0^t P_{in} - P_{out}\,dt \\ &= 0.5C_{eq}\left[U_{dc}^2(t) - U_{dc0}^2\right] + 0.5L_{eq}\left[i_{dc}^2(t) - i_{dc0}^2\right]\end{aligned} \tag{14}$$

Where ΔW_{MMC} is the converter surplus energy, $U_{dc}(t)$ and U_{dc0} are the DC voltages during and before the fault, respectively, $i_{dc}(t)$ and $i_{dc0}$are the DC currents during and before the fault, respectively, C_{eq} is the equivalent capacitance of the converter, and L_{eq} is the equivalent arm inductance of the converter.

Since the arm inductance is relatively small, the energy fluctuation on the arm inductors is negligible compared with the energy variation of the submodule capacitors. Therefore, Eq. (14) can be simplified as

$$\Delta W_{MMC} = 0.5C_{eq}\left[U_{dc}^2(t) - U_{dc0}^2\right] \tag{15}$$

Differentiating Eq. (15) yields the unbalanced power ΔP of the faulty converter:

$$\Delta P = \frac{d(0.5C_{eq}\left[U_{dc}^2(t) - U_{dc0}^2\right])}{dt} \tag{16}$$

Using the unbalanced power as a dynamic correction term for the power setpoint enables its dynamic adjustment according to the fault severity. The

resulting power reduction control loop is shown in Fig. 7.In Fig. 7, G is the inertia transfer coefficient, T is the time constant of the low-pass filter, $P_{\text{ref,pu}}$ is the steady-state active power setpoint, and $P_{\text{ref1,pu}}$ is the active power setpoint during faults.

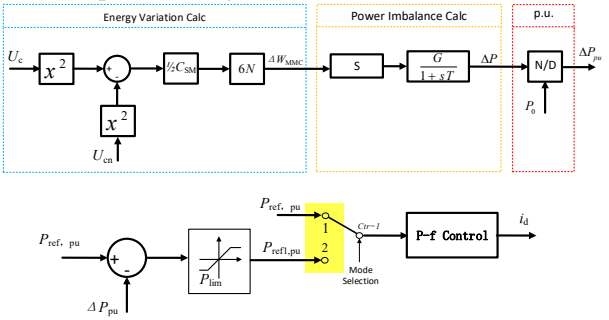


Fig. 7. Additional control block diagram of the active power-frequency loop

To prevent the new power setpoint from becoming too low under severe faults, which would make it impossible to operate on Curve 2 after fault clearance, a limiting link should be incorporated to ensure that the active power setpoint does not fall below the power limit P_{lim}, regardless of fault severity. The expression for P_{lim} is obtained from Eq. (10):

$$P_{\text{lim}} == P_{\text{sm}} \sin(\delta_A^{'} + 90^{\circ}) \tag{17}$$

In steady-state operation, Mode 1 is active with the switch at Position 1, and the MMC active power setpoint is $P_{\text{ref, pu}}$.When a fault occurs in the receiving-end AC system, Mode 2 is activated with the switch at Position 2, and the MMC power setpoint becomes $P_{\text{ref1, pu}}$. After fault clearing, Mode 1 is restored with the switch at Position 1. The MMC active power setpoint returns to $P_{\text{ref, pu}}$, and the active power is rapidly regulated back to its steady-state value, thereby restoring DC system stability.

The P-f control takes the difference between the original power setpoint and the unbalanced power of the converter during the fault as the new active power setpoint, yielding a revised virtual power angle curve, as shown in Fig. 8.Comparison of the virtual power angle curves before and after the power reduction shows that this strategy achieves smooth power reduction, avoiding additional disturbances to the system. Moreover, while increasing the CCA and reducing the deceleration area, it maintains the equality between the acceleration and deceleration areas. The dynamic reduction of the power setpoint also lowers the inner-loop current reference, which facilitates system recovery.

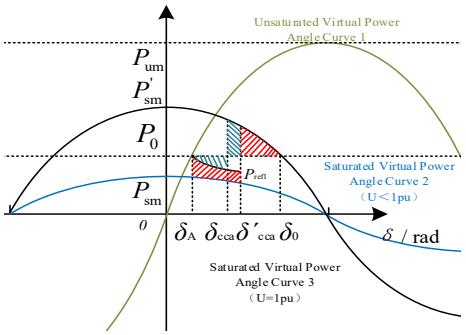


Fig.8. Virtual power angle curves of the converter after power reduction

C. Smooth Switching Control Between GFL and GFM

The preceding analysis indicates that GFM control faces the risk of instability under severe faults when the virtual power angle exceeds the CCA. In contrast, GFL control, with its PLL synchronization and fast power tracking capability, exhibits more reliable transient response during fault ride-through. To leverage the complementary advantages of the two control modes, a transition from GFM to GFL control is required when the fault evolves to a critical state, with the switching criterion being whether the virtual power angle exceeds the CCA. During normal operation, the converter operates in GFM mode. After a fault, if the virtual power angle remains below the CCA when the fault is cleared, the system restores stability and stays in GFM mode. If the virtual power angle exceeds the CCA and the fault persists, the system will experience transient instability and must switch from GFM to GFL control. Once stability is restored, the system switches back to GFM mode.

When the converter operates in GFM mode, the inner-loop current reference is generated through virtual admittance control, which converts $E\angle\delta'$ derived from the VSG control and Q-V control. When the converter operates in GFL mode, the inner-loop current reference is generated through constant active power and constant reactive power control. The difference in outer-loop control during switching causes an abrupt change in the inner-loop current reference, affecting system stability. To address this issue, the continuity of the inner-loop current references $i_{d\text{ref}}$ and $i_{q\text{ref}}$ must be ensured before and after switching.

To this end, a smooth switching link with feedforward compensation is designed, which enables the backup controller to track the output of the main controller in real time, thereby ensuring that $i_{d\text{ref}}$ and $i_{q\text{ref}}$ remain synchronized during transitions between

GFL and GFM controls. Taking GFM as the main controller and GFL as the backup controller as an example, the block diagram of the d-axis control is shown in Fig. 9.

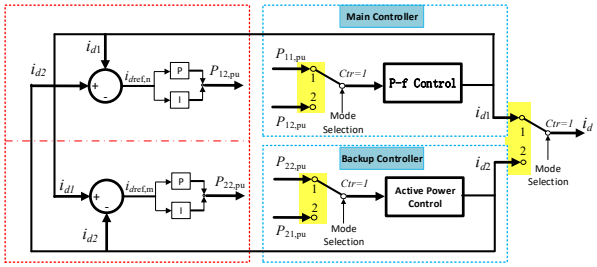


Fig. 9. Smooth switching control block diagram of the d-axis control

During steady-state operation, the difference between i_{d1} (generated by the main controller) and i_{d2} (generated by the backup controller) is obtained, and the resulting deviation $i_{\mathrm{dref,m}}$ is fed through a PI loop to generate the backup feedforward term $P_{22,\mathrm{pu}}$.Meanwhile, the difference between i_{d2} and i_{d1} yields the deviation $i_{\mathrm{dref,n}}$, which is fed through a PI loop to generate the main feedforward term $P_{12,\mathrm{pu}}$. Initially, Mode 1 is active with the switch at Position 1: the constant active power control receives the measured value $P_{21,\mathrm{pu}}$, while the backup control receives the feedforward term $P_{22,\mathrm{pu}}$.When the virtual power angle of the VSG is detected to exceed the CCA, the converter control mode switches from GFM to GFL, and the switch is set to Position 2, i.e., the main control receives the feedforward term$P_{12,\mathrm{pu}}$, while the backup control receives the measured value $P_{11,\mathrm{pu}}$.Subsequently, the converter operates under constant active power control. The feedforward terms establish a negative feedback loop between i_{d1} and i_{d2}, ensuring the continuity of the d-axis inner-loop current references before and after switching.

Taking the d-axis control as an example, the mathematical model is given by Eq. (18):

$$\begin{cases} i_{d2} = (k_{\mathrm{p22}} + \dfrac{k_{i22}}{s})\ (P_{22} - P_{\mathrm{out}}) \\ P_{22} = (i_{d1} - i_{d2})(k_{\mathrm{p21}} + \dfrac{k_{i21}}{s}) \end{cases} \tag{18}$$

By separating i_{d1} and i_{d2} in Eq. (18), Eq. (19) is obtained:

$$\begin{cases} i_{d2} = \dfrac{\partial}{\partial + 1} i_{d1} - \dfrac{(k_{\mathrm{p22}} + \dfrac{k_{i22}}{s})}{\partial + 1} P_{\mathrm{out}} \\ \partial = (k_{\mathrm{p21}} + \dfrac{k_{i21}}{s})\quad (k_{\mathrm{p22}} + \dfrac{k_{i22}}{s}) \end{cases} \tag{19}$$

During steady-state operation, the active power P_{e} can be regarded as constant; thus, from Eq. (19), the steady-state relationship of the closed-loop control link is given by:

$$\lim_{t\to\infty} i_{d2} = \lim_{s\to 0}[\frac{\partial}{\partial + 1} i_{d1} - \frac{(k_{\mathrm{p22}} + \dfrac{k_{i22}}{s})}{\partial + 1} P_{\mathrm{out}}] = i_{d1} \tag{20}$$

From Eq. (20), under steady-state operation, $i_d = i_{d1} = i_{d2}$ can be achieved, and the same holds for q-axis current control. The smooth switching link and operation of the q-axis control strategy are similar to those of the d-axis control. The block diagram is shown in Fig. 10.

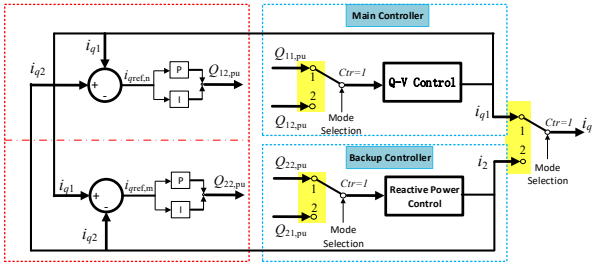


Fig. 10. Smooth switching control block diagram of the q-axis control

During steady-state operation, the difference between i_{q1} (generated by the main controller) and i_{q2} (generated by the backup controller) is obtained, and the resulting deviation $i_{\mathrm{qref,m}}$ is fed through a PI loop to generate the backup feedforward term $Q_{22,\mathrm{pu}}$.

Meanwhile, the difference between i_{q2} and i_{q1} yields the deviation $i_{\mathrm{qref,n}}$, which is fed through a PI loop to generate the main feedforward term $Q_{12,\mathrm{pu}}$.Initially, Mode 1 is active with the switch at Position 1: the constant reactive power control receives the measured value $Q_{11,\mathrm{pu}}$, while the backup control receives the feedforward term $Q_{22,\mathrm{pu}}$.When the virtual power angle of the VSG exceeds the CCA, the converter control mode switches from GFM to GFL, and the switch is set to Position 2, i.e., the main control receives the feedforward term $Q_{12,\mathrm{pu}}$, while the backup control receives the measured value $Q_{21,\mathrm{pu}}$.Subsequently, the converter operates under constant reactive power control. The feedforward terms establish a negative feedback loop between i_{q1} and i_{q2}, ensuring the continuity of the q-axis inner-loop current references before and after switching.

V. Simulation Verification

A. *Verification of Critical Instability Characteristics of Virtual Power Angle*

To validate the impact of the virtual power angle exceeding the CCA on system transient stability under GFM control, an electromagnetic transient simulation model is built in PSCAD. A three-phase short-circuit fault is applied to the high-end converter AC bus at t = 5 s, causing the voltage to drop to 0.4 p.u., with fault clearing at t = 5.6 s and t = 5.7 s, respectively. Fig. 11 presents the simulated electrical quantities of the

converter under GFM control for fault clearing at t = 5.6 s and t = 5.7 s, respectively.

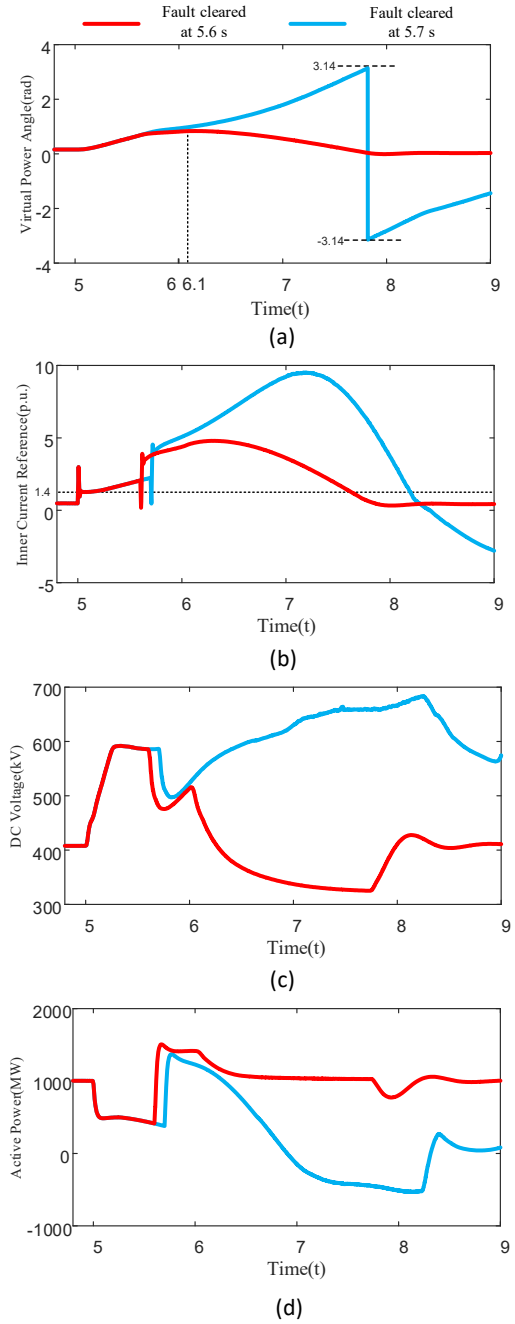
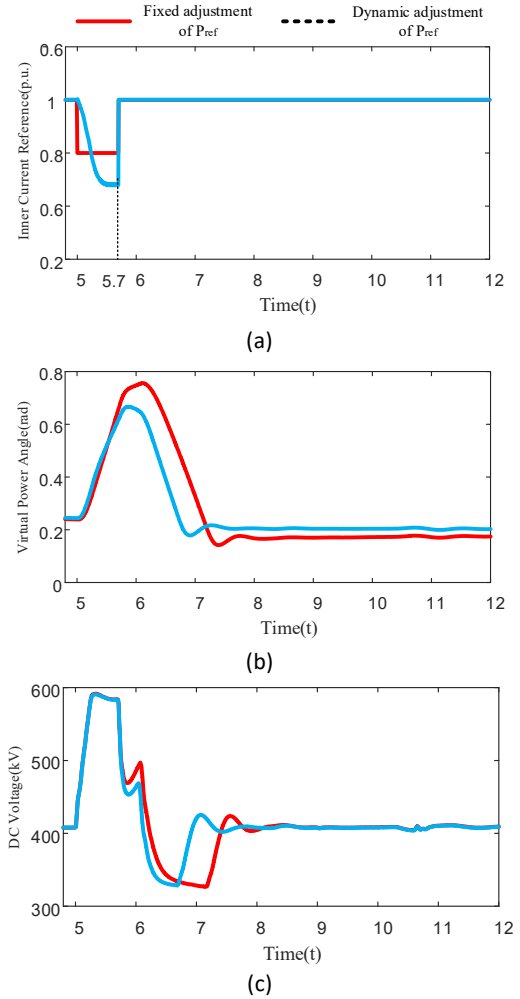


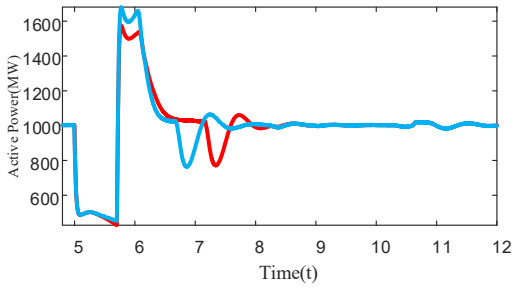
Fig. 11. Comparison of electrical quantities under different fault clearing times

As shown in Fig. 11(b), when the AC bus voltage drops to 0.4 p.u., the d-axis inner-loop current references exceed the limiting value, and the external characteristic of the faulty converter changes from a voltage source to a current source. As shown in Fig. 11(a), the virtual power angle continues to rise. If the fault is cleared at t = 5.6 s, the virtual power angle does not exceed the CCA; due to inertia, it rises until t = 6.1 s and then gradually restores stability. If the fault is cleared at t = 5.7 s, the virtual power angle exceeds the CCA and continues to increase. As observed in Figs. 11(c) and (d), the active power drop and DC overvoltage during the fault are essentially identical under both conditions due to the activation of the current limiting. However, when the fault is cleared at t = 5.6 s, the DC voltage and active power recover to stable values by t = 9 s; when cleared at t = 5.7 s, they do not stabilize until t = 12 s. Moreover, during the recovery period, the overvoltage reaches as high as 1.8 p.u., posing a potential threat to system security.

B. Simulation Verification of Dynamic Power Reduction Control Strategy

To validate the effectiveness of the proposed P-f supplementary control in increasing the CCA and extending the CCT, and to compare its advantages over the fixed power setpoint scheme, a three-phase short-circuit fault is applied to the high-end converter AC bus at t = 5 s, causing the voltage to drop to 0.4 p.u., with the fault cleared at t = 5.7 s. Fig. 12 presents a comparison of the electrical quantities under two conditions: with the proposed supplementary control (dynamic power setpoint adjustment) and with a fixed power setpoint of 0.8 p.u.



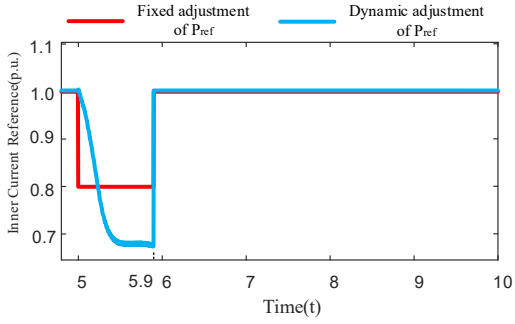


(d)

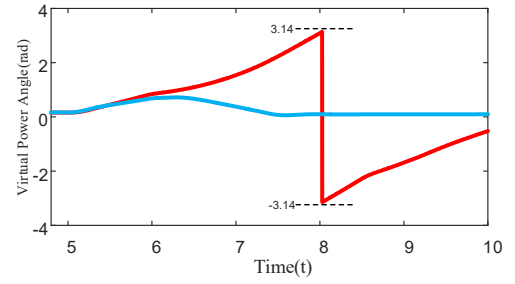
Fig. 12. Comparison of electrical quantities with fixed/dynamic power setpoint adjustment when fault cleared at 5.7 s

As shown in Fig. 12, with fault clearing at t = 5.7 s in both cases, the system remains stable with the adjusted power setpoint. Both conditions restore stability after fault clearing. However, as shown in Fig. 12(b), with the supplementary control, the virtual power angle gradually decreases and restores stability after t = 5.9 s due to inertia, while under the fixed power reduction scheme, it does not begin to recover until t = 6.15 s. This is because the supplementary control dynamically adjusts the power setpoint according to the fault severity, resulting in a smaller acceleration area and thus a shorter inertia period after fault clearing.

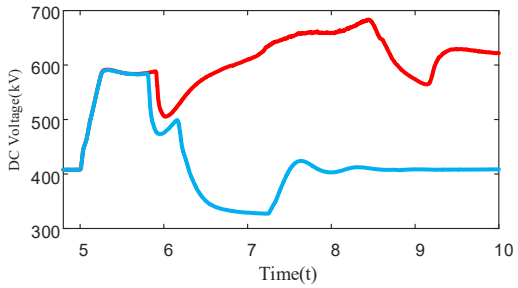
As observed in Figs. 12(c) and (d), with the supplementary control, the DC voltage and active power recover to stable values at t = 8 s, whereas the fixed power reduction scheme experiences a delay of about 0.5 s in recovery.



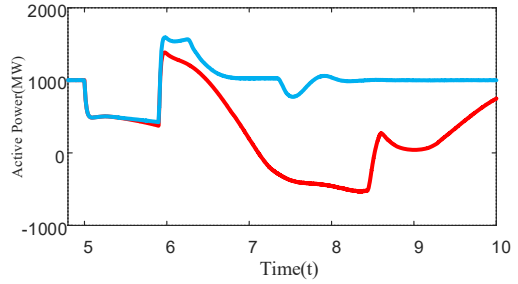
(a)



(b)



(c)



(d)

Fig. 13. Comparison of electrical quantities with fixed/dynamic power setpoint adjustment when fault cleared at 5.9 s

As shown in Fig. 13, when the fault clearing time is extended to t = 5.9 s, the system becomes transiently unstable under the fixed power reduction scheme. As observed in Fig. 13(b), under the fixed power reduction scheme, the virtual power angle continues to increase after fault clearing and fails to restore stability. In contrast, with the supplementary dynamic power reduction, although the virtual power angle rises further due to inertia, it begins to decline at approximately t = 6.2 s and returns to the steady-state value at t = 7.5 s. This is because under the fixed power reduction scheme, the power setpoint remains unchanged during the fault and does not vary with fault severity, so the acceleration area remains larger than the deceleration area, causing the virtual power angle to exceed the CCA. In contrast, dynamic power reduction adjusts the setpoint based on surplus power, effectively reducing the acceleration area and enabling the system to maintain stability even with a later fault clearing time. As observed in Figs. 13(c) and (d), under the dynamic power reduction scheme, the DC voltage peak is approximately 590 kV, and the active power drops to 380 MW before recovering at t = 8.5 s. Under the fixed power reduction scheme, however, the DC voltage continues to rise to 690 kV after fault clearing, and the active power oscillates severely and fail to recover.

In summary, the proposed dynamic power reduction strategy based on surplus power provides a larger transient stability margin compared with the fixed power reduction scheme. Even with delayed fault

clearing, it can effectively prevent the GFM converter from being locked in current-source mode, thereby ensuring secure system operation.

C. *Simulation Verification of Smooth Switching Control Between GFL and GFM*

To verify the effectiveness of switching converters I and IV from GFM to GFL control via the smooth switching link when the virtual power angle exceeds the CCA during a fault is beneficial to system recovery, a three-phase short-circuit fault is applied to the high-end AC bus at t = 5 s, causing the voltage to drop to 0.1 p.u., with the fault cleared at t = 5.6 s. Fig. 14 presents the simulated DC voltage, active power, and inner-loop current reference of Converter I during the fault.

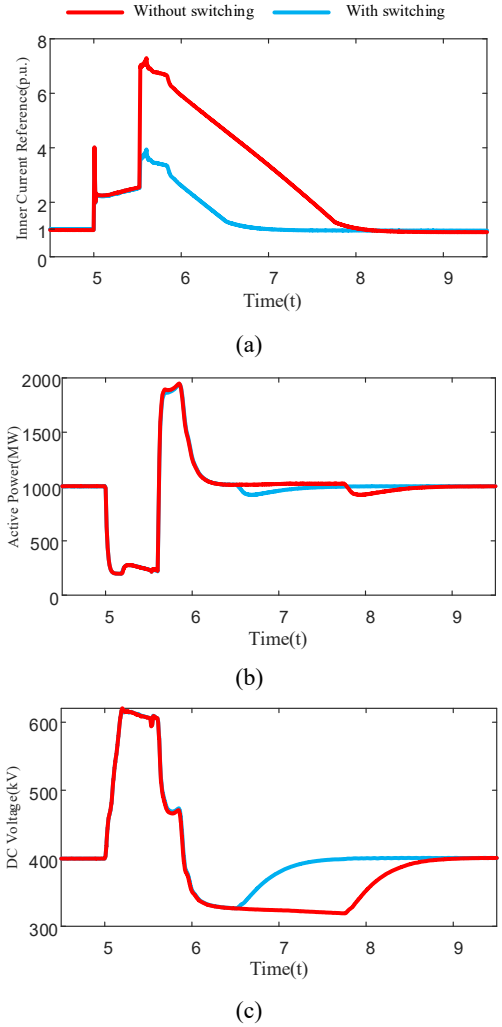


Fig. 14. Comparison of electrical quantities with and without smooth switching control during transient period

As shown in Fig. 14, upon detecting that the virtual power angle exceeds the CCA, converters I and IV switch from GFM to GFL control. This prevents the converter from being locked in current-source mode under GFM control, thereby avoiding transient instability. As shown in Fig. 14(c), the system restores stability at t = 7.5 s. Without the smooth switching link, the inner-loop current reference decreases slowly, delaying the recovery of active power and DC voltage. With the smooth switching link, the transient process prolongation caused by control switching is significantly reduced, and the recovery time is shortened by 1 s.

VI. CONCLUSION

This paper has addressed the transient instability issue of GFM control in an LCC-MMC UHVDC hybrid transmission system with hierarchical connection at the receiving end under AC faults, and proposed an optimized control strategy based on the virtual power angle. The main conclusions are as follows:

1）The evolution mechanism of the virtual power angle in GFM converters before and after current limiting is revealed, and the transient instability conditions under which the converter becomes locked in current-source mode are identified. using the equal-area criterion, the analytical expression of the CCA is derived, which shows that the CCA decreases with an increase in the active power setpoint.

2）A dynamic power reduction control strategy based on surplus power is proposed, which uses the unbalanced power at the converter station during a fault to dynamically adjust the power setpoint of the P-f control loop in real time, thereby increasing the CCA. Simulation results show that, compared with the fixed power reduction scheme, this strategy exhibits smaller transient disturbances, shorter power recovery time, and a larger transient stability margin.

3）A smooth switching control strategy based on the virtual power angle criterion is proposed for transitions between GFL and GFM modes. A feedforward compensation loop ensures the continuity of the inner-loop current reference at the switching instant. When the virtual power angle exceeds the CCA, the system smoothly switches to GFL control, preventing the converter from being locked in current-source mode and significantly enhancing the fault ride-through capability under severe faults.

The proposed method achieves complementary advantages. It combines the active voltage and frequency support of GFM control under steady-state conditions with the fault ride-through capability of GFL control during faults. Future work will further consider the interactive coupling effects between sending-end

and receiving-end faults, as well as the adaptive optimization of control parameters.

DECLARATIONS

Data availability：All data generated or analysed during this study are included in this published article and its figures.

Competing interests: I declare that the authors have no competing interests as defined by Springer, or other interests that might be perceived to influence the results and/or discussion reported in this paper.

Research Funding：This work was supported by the State Grid Hebei Electric Power Research Institute under Grant No. kj2025-028.

Author Contributions Statement： W.M.Z. and Q.Q.L. conceived the original idea and designed the overall research framework. W.M.Z. derived the theoretical formulations and drafted the main manuscript text. Q.Q.L. developed the dynamic power reduction control strategy and the smooth switching control scheme. Y.L.C. and S.F.G. carried out the PSCAD/EMTDC simulation model construction and performed the simulation studies. Z.L. analyzed the simulation data and prepared all the figures. All authors reviewed the manuscript and approved the final version.

REFERENCES

[1] S. M. A. Halim, T. D. C. Busarello, F. A. Khan, et al., "Improved control strategy of current-source converter for HVDC system," *IEEE Access*, vol. 11, pp. 1-18, 2023.

[2] S. Lu, H. Pan, X. Jia, et al., "AC fault ride-through strategy of constant power MMC in UHV hybrid three-terminal DC transmission system," *J. North China Electr. Power Univ. (Nat. Sci. Ed.)*, vol. 51, no. 2, pp. 11-22, 2024.

[3] D. Yang, S. Sun, Y. Sun, et al., "Analysis of typical AC/DC fault characteristics at the receiving end of hybrid cascaded HVDC transmission system," *J. Shandong Univ. (Eng. Sci.)*, vol. 53, no. 6, pp. 131-142, 151, 2023.

[4] W. Li, M. Ma, and W. Sun, "Frequency oscillation characteristic analysis of grid-forming multi-VSG system considering power coupling," *Electr. Power Eng. Technol.*, vol. 44, no. 2, pp. 44-54, 2025.

[5] M. M. Esfahani, S. A. Hosseini, M. Moallem, et al., "A comparative analysis of grid-following and grid-forming control techniques used in inverter-based resources," in *Proc. 2025 IEEE 4th Int. Conf. Smart Energy Grid Eng. (SEGE)*, Oshawa, ON, Canada, 2025, pp. 1-6.

[6] H. Xin, Y. Yang, and Q. Fu, "Grid-forming technology actively supports operation and control of new power systems," *Electr. Power Eng. Technol.*, vol. 44, no. 2, pp. 2-3, 2025.

[7] Z. Chen, L. Yang, J. Shi, et al., "Transient stability analysis of grid-forming converter paralleled with grid-following converter system considering transient mode switching," *Proc. CSEE*, vol. 45, no. 15, pp. 6025-6038, 2025.

[8] Y. Lin, W. Li, L. Zhu, et al., "A review of transient control strategies for grid-forming converters under grid voltage sags," *Electr. Power Eng. Technol.*, vol. 44, no. 2, pp. 55-68, 2025.

[9] J. Xu, W. Liu, S. Liu, et al., "Current state and development trends of grid-forming control technology for power system converters," *Power Syst. Technol.*, vol. 46, no. 9, pp. 3586-3595, 2022.

[10] C. Zhan, H. Wu, X. Wang, et al., "A review of stability research on grid-forming converters," *Proc. CSEE*, vol. 43, no. 6, pp. 2339-2359, 2023.

[11] Y. Zhang, C. Zhang, X. Cai, et al., "Research on transient voltage support mechanism with current limitation and improved fault ride-through control for virtual synchronous generators," *Proc. CSEE*, vol. 44, no. 15, pp. 5996-6010, 2024.

[12] Y. Lu, Y. Li, D. Yang, et al., "Transient synchronization stability analysis of multi-VSG system considering controller limits," *Autom. Electr. Power Syst.*, vol. 49, no. 7, pp. 25-34, 2025.

[13] L. Huang, L. Zhang, H. Xin, et al., "Analysis on virtual power angle stability mechanism of droop-controlled inverters," *Autom. Electr. Power Syst.*, vol. 40, no. 12, pp. 117-123, 150, 2016.

[14] Y. Li, S. Zhao, D. Cai, et al., "Transient synchronization stability analysis of grid-forming renewable energy delivered via VSC-HVDC system under current-limiting constraints," *High Voltage Eng.*, vol. 51, no. 9, 2025. (in press)

[15] W. Chao, G. Lin, L. Dai, et al., "A commutation failure suppression strategy applicable to the UHVDC hierarchical connection system," *Mod. Electr. Power*, vol. 40, no. 6, pp. 1060-1067, 2023.

[16] X. Tong, "Research on application of VSC-HVDC technology in wind power grid connection," M.S. thesis, Lanzhou Jiaotong Univ., Lanzhou, China, 2023.

[17] P. Wang, P. Wang, S. Li, et al., "Dynamic current-limiting control strategy for grid-forming inverter under grid faults," *High Voltage Eng.*, vol. 48, no. 10, pp. 3829-3837, 2022.

[18] Power System Technology，2019, 43(09)：3408-3414．A. Zheng, C. Guo, P. Cui, et al., "Voltage balance control strategy between series-connected converter valve groups in UHVDC hybrid multi-terminal DC transmission systems," *Power Syst. Technol.*, vol. 43, no. 9, pp. 3408-3414, 2019.

[19] B. Zhang, X. Wang, F. Zhao, et al., "Asymmetric impedance model for grid-forming converters with droop control," *IEEE Trans. Power Electron.*, vol. 40, no. 6, pp. 1-12, 2025.

[20] D. Zhang, Y. Sui, X. Hu, et al., "Analysis of similarities and differences in stability between virtual impedance and virtual admittance control for grid-forming SVG," *Adv. Technol. Electr. Eng. Energy*, vol. 44, no. 11, pp. 97-108, 2025.

[21] G. Wang, L. Fu, Q. Hu, et al., "Transient synchronization stability of grid-forming converter during grid fault considering transient switched operation mode," *IEEE Trans. Sustain. Energy*, vol. 14, no. 3, pp. 1504-1515, 2023.

[22] N. Zhang, Z. Xu, and Z. Zhang, "Fault ride-through control strategy of receiving-end AC system in LCC-FHMMC hybrid HVDC transmission system," *Electr. Power Autom. Equip.*, vol. 43, no. 4, pp. 39-45, 53, 2023.



Weiming Zhang is currently a Senior Engineer with the State Grid Hebei Electric Power Research Institute, Shijiazhuang, China. His research interests include control and protection of HVDC transmission systems. (E-mail: 858436030@qq.com)

Qingquan Liu is currently a Senior Engineer with the State Grid Hebei Electric Power Research Institute, Shijiazhuang, China. His research interests include power system protection and control. (E-mail: liuqingquan0311@163.com)